Geophysical Research Letters

RESEARCH LETTER
10.1029/2018GL080523

Special Section:
50 years of Apollo Science

Time-Dependent Hybrid Plasma Simulations of Lunar Electromagnetic Induction in the Solar Wind

H. Fuqua Haviland[1], A. R. Poppe[2,3], S. Fatemi[4], G. T. Delory[2,3], and I. de Pater[5]

[1]NASA Marshall Space Flight Center, Huntsville, AL, USA, [2]Space Sciences Laboratory, University of California, Berkeley, CA, USA, [3]Solar System Exploration Research Virtual Institute, NASA Ames Research Center, Moffett Field, CA, USA, [4]Swedish Institute of Space Physics, Kiruna, Sweden, [5]Earth and Planetary Science Department, University of California, Berkeley, CA, USA

Key Points:
- A time-dependent hybrid plasma model studies the interaction of induced magnetic fields and the lunar plasma environment
- Induced magnetic fields from the lunar interior self-consistently couple with ambient plasma and thereby differ from analytic predictions
- Coupling of plasma interaction with induction must be accounted for in electromagnetic sounding studies of airless bodies

Correspondence to:
H. Fuqua Haviland,
heidi.fuqua@berkeley.edu

Citation:
Fuqua Haviland, H., Poppe, A. R., Fatemi, S., Delory, G. T., & de Pater, I. (2019). Time-dependent hybrid plasma simulations of lunar electromagnetic induction in the solar wind. *Geophysical Research Letters*, *46*, 4151–4160. https://doi.org/10.1029/2018GL080523

Received 17 SEP 2018
Accepted 25 MAR 2019
Accepted article online 28 MAR 2019
Published online 17 APR 2019

Abstract Understanding the structure and composition of the lunar interior is fundamental to furthering our knowledge of the formation and subsequent evolution of the Earth-Moon system. Among various methods, electromagnetic sounding is a valuable approach to constraining lunar interior structure. While Apollo-era electromagnetic sounding analyses of lunar magnetometer observations reported constraints on the lunar interior structure, the presence of perturbing plasma currents and magnetic fields was often regarded as a second-order correction. Here, we use AMITIS, a three-dimensional, time-dependent hybrid plasma model with a conducting lunar interior to demonstrate that electromagnetic fields from the lunar wake and from the lunar interior interact and thereby alter geophysically induced electromagnetic fields. Our results indicate that electromagnetic sounding of airless bodies interacting with a conductive plasma and exposed to a time-varying magnetic field must be interpreted via plasma models in order to untangle plasma and induced field contributions.

Plain Language Summary Magnetic field observations near the Moon can be used to remotely detect the interior. These observations can be related back to composition, structure, and temperature. This technique was applied during Apollo using a surface magnetometer and in orbit. When the Moon is outside of the Earth's magnetic field, the lunar surface interacts directly with the solar wind plasma particles from the Sun. The Moon's presence interrupts this steady flow of plasma by absorbing particles on the sunlit side, while a region of no particles forms on the opposite side. This plasma wake generates its own magnetic fields that interact with interior fields. In order to understand any contribution to the observations, we apply a new computer simulation, which solves first principles equations to determine the plasma wake and interior fields in three dimensions and in time. This novel technique provides a new understanding of the Moon-plasma magnetic field interaction and improves previous models that neglected this interaction. Previous interpretations assumed any interior fields on the nightside were trapped within the plasma wake cavity; however, we see these magnetic fields are coupled with the wake magnetic fields. This is applicable to any airless body in a similar space-plasma environment.

1. Introduction

Understanding the current composition, state, and structure of the lunar interior provides vital insight into the history of the Moon including its origin and potential formation processes (e.g., Canup et al., 2015; Ćuk et al., 2016; Jaumann et al., 2012; Lock & Stewart, 2017; Lock et al., 2018). The Moon has a highland plagioclase flotation crust with a bulk density of 2,550 kg/m^3, an average thickness between 34 and 43 km, and a porosity of 12%; however, the nearside and farside hemispheres exhibit disparate crustal thickness values of over 60 km (Wieczorek et al., 2006, 2013). The crust is observed to be highly resistive with an electrical conductivity of order 10^{-9} S/m (Dyal et al., 1974); however, the nearside maria Procellarum KREEP Terrane is enriched in radioactive concentrations and has a corresponding enhancement in electrical and thermal conductivity (Grimm, 2013; Jolliff et al., 2000). The mantle possesses an electrical conductivity within the range 10^{-4} to 10^{-3} S/m (Dyal et al., 1976), and previous electromagnetic (EM) sounding analyses by the Apollo (Dyal et al., 1976; Russell et al., 1981), Lunar Prospector (Hood et al., 1999), and Kaguya (Shimizu et al., 2013) missions have constrained the presence of a conducting core to be less than ≈430 km in thickness with a conductivity greater than 10^{-2} S/m (Dyal et al., 1976); however, Hood et al. (1999) notes

that their analysis is also consistent with no lunar core due to weak constraints. More recently, a reanalysis of Apollo seismic data has suggested the presence of a differentiated lunar interior and a differentiated iron core enriched in light elements of less than 6% by weight, consistent with smaller core models of 330 ± 20 km (Weber et al., 2011). Nevertheless, despite 40 years of investigations, the full thermal and conductive structure of the lunar interior remains an open question.

EM sounding is a geophysical method of constraining the electrical conductivity and temperature of a solid body interior through observations of EM fields induced within conducting layers by changes in the ambient EM environment. Magnetic field observations at or near the surface, containing the total field, as well as a reference observation outside of any induced effects, are compared against models that solve for the induced response in terms of interior electrical conductivity and boundary conditions (e.g., Blank & Sill, 1969; Dyal & Parkin, 1971; Grimm & Delory, 2012; Schubert & Schwartz, 1969). At the Moon, the ambient EM environments include the solar wind, the terrestrial magnetosheath, and the terrestrial magnetotail (e.g., Halekas et al., 2011, and ref. therein). When in the solar wind (≈75% of a lunar orbit), the absorption of supersonic solar wind ions by the lunar dayside surface causes the formation of the lunar wake, a region of low-density plasma that extends at least 10 lunar radii downstream (e.g., Kallio, 2005; Holmström et al., 2012). The presence of a deep vacuum within the lunar wake induces a complex set of currents and associated perturbative magnetic fields around the various boundaries of the wake (e.g., Fatemi et al., 2013; Vernisse et al., 2013; Zhang et al., 2012, 2014). In turn, these plasma-induced fields may alter and/or obscure any geophysically induced EM fields from the lunar interior. Indeed, plasma interaction models for objects such as asteroids (e.g., Oran et al., 2018), the Moon (albeit without time-dependent fields; e.g., Wang et al., 2011), Mercury (e.g., Jia et al., 2015), and the outer planet satellites (e.g., Lindkvist et al., 2015; Lipatov et al., 2013; Khurana et al., 2009, 2011) have shown the importance of including induced fields from planetary interiors.

Early in the development of EM sounding theory at the Moon, a full understanding of the interaction between the wake fields and any geophysically induced fields from the conducting lunar interior was identified as a challenge (Sonett & Colburn, 1967, 1968). To overcome this, Dyal and Parkin (1971) made the assumption that induced magnetic fields would expand unimpeded into the lunar wake as if in a vacuum; however, others criticized this method for not considering the role that ambient plasma interactions may play in altering the induced EM signals (Schubert et al., 1973; Schwartz & Schubert, 1973). In particular, Schubert et al. (1973) stated that the interpretation of nightside observations within a time domain EM (TDEM) sounding analysis should await a model capable of capturing the full asymmetric induced response. More recently, Fatemi et al. (2015) studied the time-*independent* interaction between induced fields from the lunar interior and plasma wake fields within the nightside cavity by placing a static dipole of varying strength within the lunar interior in order to mimic the presence of induced fields. In particular, Fatemi et al. (2015) found that the induced fields were not necessarily confined by the plasma wake cavity as previously proposed (e.g., Dyal & Parkin, 1971; Sonett, 1982) and that induced fields could extend beyond the traditional boundary of the lunar wake. A region was found in the models where the induced field is minimally disturbed by the wake or plasma interactions at the surface antisubsolar point; however, the time-independent nature of the hybrid model used in Fatemi et al. (2015) left open the question of whether or not these features were also present in the more realistic, time-dependent case.

Here, we analyze the time-dependent induced magnetic field response of the Moon as predicted by a three-dimensional hybrid model of the lunar plasma interaction with a conducting lunar interior responding to an upstream interplanetary magnetic field (IMF) discontinuity within the solar wind. We compare simulation results using three values of the effective lunar conductivity with the analytic theory of Dyal and Parkin (1971) for a transient response.

2. Model Description

In order to simulate the self-consistent interaction of the solar wind with the Moon and to model the formation of time-dependent induced magnetic fields in the lunar interior, we employ AMITIS, a Graphics Processing Unit (GPU) based hybrid model of plasma that runs on a single CPU-GPU pair. As described in detail in Fatemi et al. (2017), AMITIS is a standard, three-dimensional plasma hybrid model that treats ions as individual macroparticles and electrons as a charge-neutralizing fluid. EM fields are solved on a Cartesian grid using a discretized form of Maxwell's equations. Ions are introduced at the upstream boundary with a specified distribution (here, the solar wind with a Maxwellian velocity distribution) and removed from the

simulation when they encounter either the lunar surface (which is assumed to be perfectly absorbing) or the downstream simulation boundaries. In regions of vacuum (e.g., the lunar wake), the hybrid model specifies a resistivity (e.g., 2×10^{-7} S/m outside the Moon) and locally switches to solving the magnetic diffusion equation (see Fatemi et al., 2017, for a full discussion). The model employs a right-handed coordinate system centered on the Moon with the positive x axis pointing toward the Sun, the positive z axis pointing to ecliptic north, and the y axis completing the set. For simplicity, the Moon is considered to be a perfect sphere of radius $R_L = 1{,}750$ km and the model uses cubic grid cells with size 50 km ($\approx 0.03\ R_L$). An advanced feature of the AMITIS hybrid plasma model used here is the implementation of conductive layers within the Moon, representing the lunar mantle and/or core. This feature, described in greater depth in Fatemi et al. (2017), allows the specification of conductive layers of arbitrary thickness and conductivity within the Moon. This version of AMITIS also allows changes in the upstream IMF orientation and/or strength, which drive the formation of induced poloidal magnetic fields within any specified conductive layers. We note that AMITIS has been successfully benchmarked and validated against both previous simulation efforts and in situ data/model comparisons as described fully in Fatemi et al. (2017).

For all simulations here, the model maintains constant upstream solar wind particle conditions with a single rotation in the IMF. We use a simulation domain of size $-4\,R_L \leq x \leq +2\,R_L$ and $-2.3\,R_L \leq (y,z) \leq +2.3\,R_L$ with a regular-spaced Cartesian grid with cubic cells of size 50 km ($\sim 0.028\ R_L$). We use 16 macroparticles (only protons) per cell (shown to be a sufficient number from previous model-data comparisons; e.g., Fatemi et al., 2017; Poppe et al., 2014) and advance particle trajectories using a time step of $t = 0.001$ s, which is $\sim 10^{-4}$ of the solar wind proton gyroperiod. We ran all simulations to reach $\sim$ 300 s. Using typical solar wind values at 1 au, the density and velocity were set to be 6 cm^{-3} and 320 km/s, respectively, and the solar wind ion and electron temperatures were both assumed to be $\sim$ 8.5 eV. These parameters were held constant throughout the simulation time period. Upon initiation of each simulation, the interplanetary magnetic field is assumed constant throughout the domain, including within the interior of the Moon. At time $t = 0$, the IMF is [0, +4, 0] nT, and we allow the simulation to first come to steady state under these initial conditions. At $t = 24$ s, an IMF discontinuity is introduced at the upstream boundary such that the field becomes [0, −4, 0] nT (for a total change of 8 nT), which propagates downstream and interacts with both the lunar interior and the lunar wake.

We studied three cases of the lunar interior conductivity structure. In case 1, the Moon is modeled as a completely resistive sphere (conductivity of 10^{-8} S/m), in order to serve as a control. This case captures the wake response with minimal to no interaction from induced fields. In cases 2 and 3, we introduce a single, homogeneous conducting layer of thickness 1,600 km ($\sim 0.91 R_M$, or $\sim$ 32 cubic simulation grid cells) with conductivity 10^{-4} and 10^{-3} S/m, respectively, leaving a resistive crust of thickness 150 km ($\sim$3 cubic simulation grid cells) with 10^{-8} S/m conductivity. For comparison, a $|\Delta B| = 8$ nT discontinuity passing through a 1,600-km radius conducting sphere corresponds to an initial induced dipole moment, $M_{ind} = 1.64 \times 10^{17}$ A·m^2 (Fatemi et al., 2015; Saur et al., 2010). Redundancy in the simulation grid cells representing the lunar crust was needed to verify the termination of any electric currents within these resistive layers, since the discretized form of Maxwell's equations (as described in Fatemi et al., 2017) can cause currents to numerically diffuse across a resistive boundary that is only one cell in thickness. The conductivity of 10^{-8} S/m used for the "resistive" crust is several orders of magnitude higher than the experimentally measured conductivity of lunar soil samples ($\sigma \approx 10^{-14} - 10^{-13}$ S/m; e.g., Kirkici et al., 1996; Strangway et al., 1972, although Dyal et al., 1977, report lunar conductivities of 10^{-9} – 10^{-8} S/m); however, such small conductivities are computationally prohibitive with the hybrid models that handle the vacuum region using resistivity (see detailed discussion in section 4.2.3 in Fatemi et al., 2017). We compared fully resistive runs of $\sigma = 10^{-8}$ S/m and $\sigma = 10^{-7}$ S/m and saw no appreciable difference in the magnetic fields within the lunar interior, demonstrating that our selected value for the crust of 10^{-8} S/m is sufficient. Our selection of 10^{-4} and 10^{-3} S/m for the internal conductivity is motivated by previous constraints on the lunar interior conductivity structure (e.g., Dyal et al., 1976; Grimm & Delory, 2012; Hood et al., 1982; Khan et al., 2006). These conductivities, along with a conductive interior size of 1,600 km, correspond to decay times of approximately 30 – 300 s, which sets the timescales of interest for this study.

3. Model Results

Figure 1 shows the magnetic field components and magnitude in both the xy and xz Selenocentric Solar Ecliptic (SSE) planes for the resistive case ($\sigma = 10^{-8}$ S/m, top), the medium conductivity case ($\sigma =$

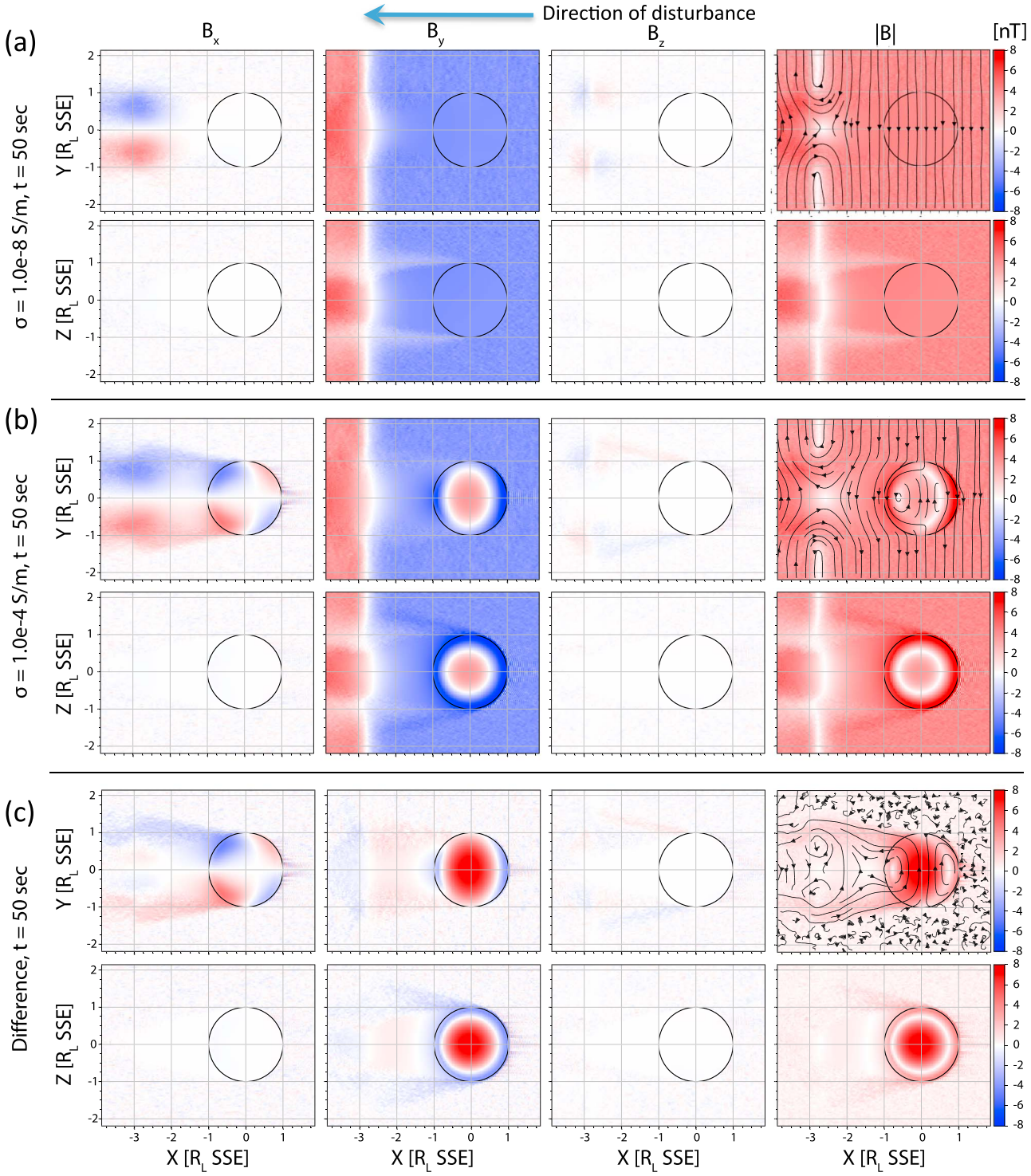

Figure 1. The magnetic field components for the resistive Moon (10^{-8} S/m; a), medium conductivity case (10^{-4} S/m; b), and residuals of the two (c) are shown in the Selenocentric Solar Ecliptic (SSE) coordinate system. The magnetic field components and magnitude are plotted in both the *xy* and *xz* planes, for a total of eight subplots per panel. All plots are for a single time step ($t = 50$ s, $x = \sim -2.8\ R_L$), 20 s after the transient event arrived at the dayside of the Moon ($x = +1\ R_L$).

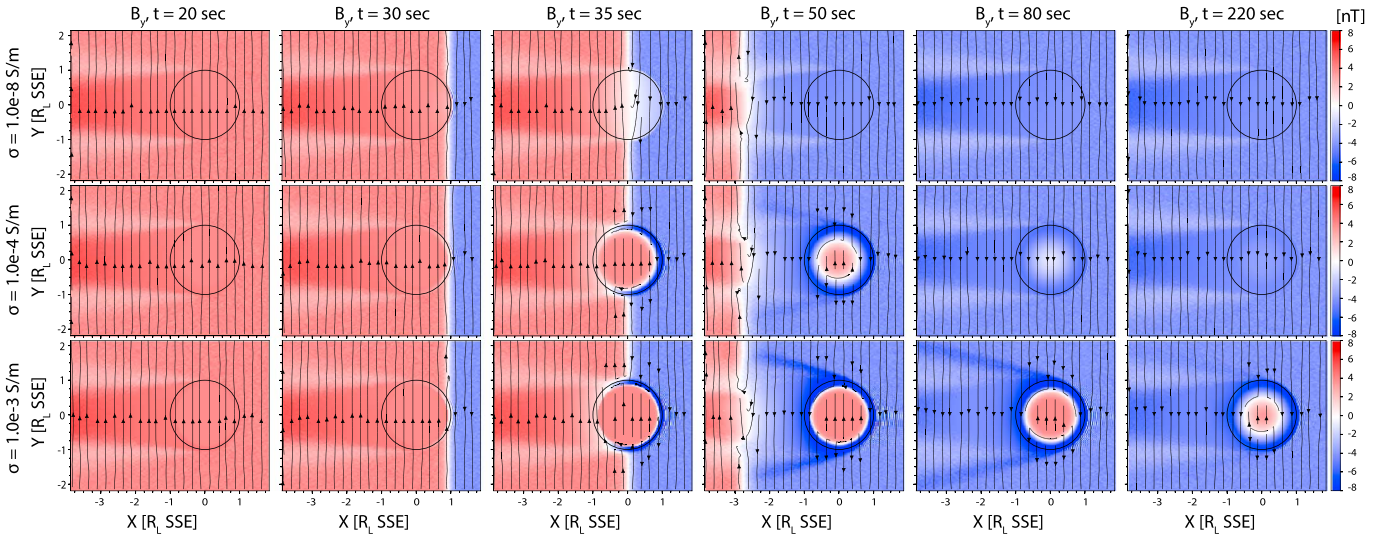

Figure 2. The magnetic field B_y component in the xz SSE plane for the three modeled conductivities (the resistive Moon 1e−8 S/m [top row], medium conductivity case 1e−4 S/m [middle row], and high conductivity case 1e−3 S/m [bottom row]), shown at six time steps. SSE = Selenocentric Solar Ecliptic.

10^{-4} S/m, middle), and the residual difference between them (bottom), 20 s after the IMF discontinuity has reached the dayside (the discontinuity can be seen at $x = -2.8\ R_L$ downstream from the Moon). This corresponds to 50 s after the start of the simulation. The resistive case captures the plasma wake dynamics with no influence from induced currents within the Moon. The discontinuity front is clearly seen in the B_y component as the transition between the positive initial field and negative final field, where the wake and its associated current systems are reconfigured to satisfy the final magnetic field conditions. Transient perturbations are also seen in the B_x and B_z components associated with the discontinuity current sheet and its interaction with the Moon. Behind the discontinuity, the simulation results show the reformation of the lunar wake, including, for example, the rarefaction boundary of the wake in B_y, xz plane, extending downstream (cf., Fatemi et al., 2013; Holmström et al., 2012).

In the medium conductivity case, shown in the two middle rows in Figure 1, an induced field from the conducting lunar interior is now present and interacts with the plasma wake fields. The differences between the resistive (Figure 1a) and conductive (Figure 1b) cases can be seen Figure 1c. The induced fields are clearly seen within the lunar interior, including a positive B_y field within approximately 0.5 R_L, an enhanced negative B_y field within approximately the outer half of the lunar interior, and field perturbations outside the lunar interior, most clearly in the B_x component in the xy plane and in the B_y component in both planes, which is due to the direction of the IMF discontinuity. The positive B_y fields deepest within the Moon are the primary induced fields generated in opposition to the $\Delta B_y = -8$ nT change in the solar wind field. The enhanced negative B_y fields within the outermost, resistive layer of the Moon are caused by the approximate confinement of the induced dipole below the lunar surface due to the solar wind pressure acting on the induced dipole. Differences in the magnetic field outside the lunar interior are due to coupling between the induced fields and the surrounding plasma and fields of the solar wind and lunar wake. Similar to the time-independent model results presented in Fatemi et al. (2015), field perturbations are seen in the B_x and B_y components along the flanks of the lunar wake. Along the lunar nightside surface, both the B_x and B_y components show distinct spatial variation with magnitudes on the order of 2 nT, or approximately 25% of the magnitude of the change in the upstream field of 8 nT.

Figure 2 compares the magnetic field y component in the xz Selenocentric Solar Ecliptic plane for all three modeled conductivities at six different time periods, $t = 20$, 30, 35, 50, 80, and 220 s, respectively. These times represent the total time elapsed since the initiation of the simulation. After 20 s, the wake structure has formed for all three lunar cases. At 30 s, the discontinuity contacts the dayside of the Moon and no differences between the three conductivity cases is yet observed; however, as the discontinuity passes by the Moon at 35 s, induced current systems form and oppose the change in the solar wind field in proportion to the interior conductivity. At 50 s, the discontinuity front is nearly three lunar radii (2.8 R_L) downstream from the Moon (i.e., the time period shown in Figure 1), and we observe distinct differences between the three lunar

conductivity cases. The top panel, with a resistive interior ($\sigma = 10^{-8}$ S/m), demonstrates the magnetic field produced by the plasma wake current systems for these solar wind conditions including a spatially constant magnetic field within the interior equal to the upstream solar wind field. The middle panel shows an induced interior response for the moderate conductivity case ($\sigma = 10^{-4}$ S/m) including a small amplification of the downstream rarefaction boundaries relative to the resistive case. Finally, the bottom panel shows the high conductivity interior case ($\sigma = 10^{-3}$ S/m) with a large interior response and amplification along the rarefaction boundary of the lunar wake. After 80 s, the discontinuity has passed far downstream and exited the simulation domain, however, induced fields are still present in both the moderate and high conductivity cases. The resistive case has reconfigured to the final magnetic field conditions, and the induced field of the medium conductivity case has nearly dissipated (< 1 nT perturbations); however, in the high conductivity case, the interior field and downstream amplification remain relatively strong (~ 3–4 nT). Even toward the end of the simulation ($t = 220$ s), the interior field remains present, albeit lower in magnitude consistent with the longer decay time associated with the larger interior conductivity; that is, the characteristic decay time for the 10^{-3} S/m case is approximately 320 s.

4. Comparison to Analytic Theory

Previous analysis of TDEM sounding for the Moon made the fundamental assumption that any induced fields were compressed below the lunar dayside surface due to solar wind ram pressure yet were simultaneously able to expand unimpeded into the lunar wake on the nightside as if in a vacuum (Dyal & Parkin, 1971). However, as pointed out by Schubert et al. (1973) and more recently modeled in a time-independent hybrid plasma models by Wang et al. (2011) and Fatemi et al. (2015), the self-consistent interaction between induced fields and the ambient solar wind plasma may in fact render this assumption inaccurate. Thus, we compare our time-dependent hybrid plasma simulation results with the theory derived in Dyal and Parkin (1971) to assess this possibility.

For a Moon with total radius R_L and a radius of internal conductivity R_1, and an upstream IMF discontinuity (defined by the difference between the initial $\mathbf{B_{Ei}}$ and final $\mathbf{B_{Ef}}$ external magnetic field, $\Delta\mathbf{B_E} = \mathbf{B_{Ef}} - \mathbf{B_{Ei}}$ with components $[\Delta\mathbf{B_{Er}}, \Delta\mathbf{B_{En}}, \Delta\mathbf{B_{Ee}}]$ in the Radial-North-East or RNE Coordinate System described below), the total magnetic field, $\mathbf{B_A} = [B_{Ar}, B_{An}, B_{Ae}]$, measured at the surface is the sum of the external and induced fields and can be expressed by components as (Dyal & Parkin, 1971)

$$B_{Ar} = -3(R_1/R_L)^3 \Delta B_{Er} F(t) + B_{Efr} \tag{1}$$

$$B_{An} = \frac{3}{2}(R_1/R_L)^3 \Delta B_{En} F(t) + B_{Efn} \tag{2}$$

$$B_{Ae} = \frac{3}{2}(R_1/R_L)^3 \Delta B_{Ee} F(t) + B_{Efe}. \tag{3}$$

This form of the equations uses the RNE local spherical coordinate system, Figure 3a, oriented at the observer location, where the radial component is normal to the surface, and the others extend tangentially to the lunar surface in the local north and east directions, respectively. The time-dependent function $F(t)$ in the above set of equations is given by

$$F(t) = \frac{2}{\pi}\sum_{s=1}^{\infty}\frac{1}{s^2}\exp\left(\frac{-s^2\pi^2 t}{\mu_o \sigma_1 R_1^2}\right), \tag{4}$$

where σ_1 is the conductivity of the interior layer and μ_o is the permeability of free space (Dyal & Parkin, 1971). Note that the characteristic decay time can be read off of equation (4) as $\tau = \mu_o \sigma_1 R_1^2/\pi^2$, assuming that the $s = 1$ term in the sum dominates the total function. As can be seen from the sign of equations (1) –(3), the radial component of the induced field opposes the change in the external radial field, while the two tangential components (east and north) add to the respective external tangential components.

Figure 3 shows the theoretical and modeled fields as a function of time by component (radial, north, and east) for all three lunar conductivity cases ((i) resistive, (ii) 10^{-4} S/m, and (iii) 10^{-3} S/m) for two specific locations: observer #1 at the anti-subsolar point (i.e., local midnight) in Figure 3b and observer #2 at 3 a.m. local time on the lunar nightside (i.e., 45° from the midnight meridian) in Figure 3c. For observer #1, the theoretical fields are solely in the east component since the change in the upstream IMF (expressed in the RNE

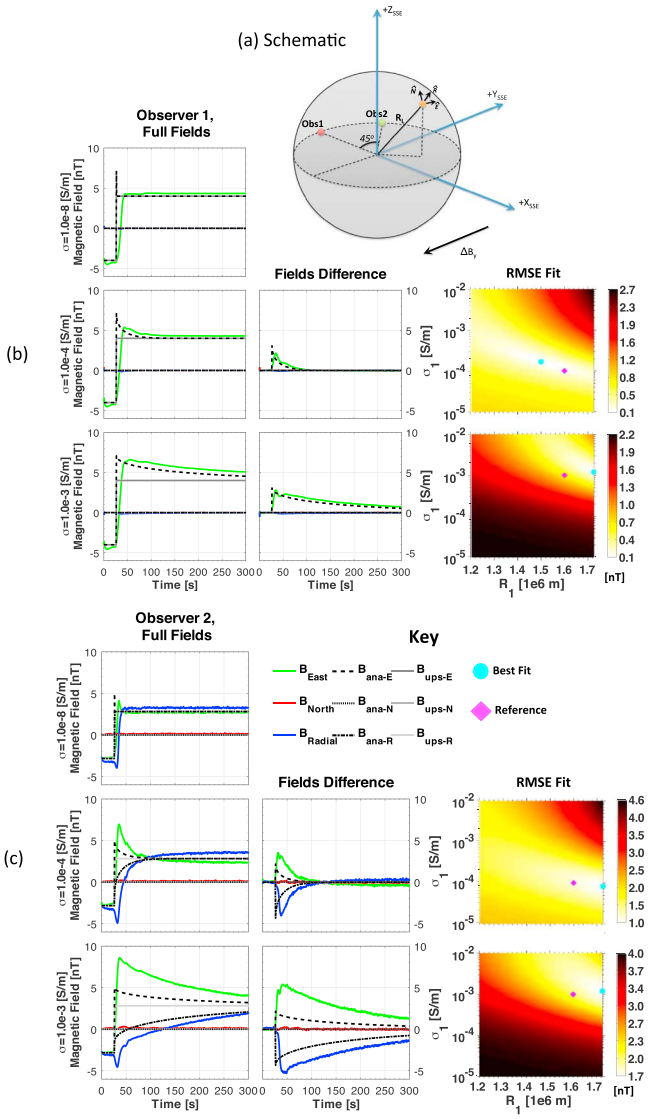

Figure 3. The time series of the magnetic field response and results of the trial sounding of each of the three simulations for both (b) Observer 1 and (c) Observer 2, respectively, as described in the text. (a) The Radial-North-East (RNE) coordinate system is depicted in the upper right-hand corner. RMSE = root-mean-square error.

coordinate system at the location of observer #1) is also solely in the east component. For this case, the hybrid simulation results approximately match the analytic predictions. In the top plot, we note that the analytic response does show a very sharp peak, corresponding to the characteristic decay time for the small but finite conductivity of the resistive case, 10^{-8} S/m. This peak is not captured by the hybrid model where the ~ 20 s time lag corresponds to the reconfiguration of the wake current systems in the east component (green curve) and the finite width of the magnetic discontinuity within the simulations. The magnetic discontinuity width is ~ $0.2R_M$ and corresponds to ~ 1 s delay. For the medium conductivity case (middle row), the model shows a very similar time decay of the east component compared to the analytic theory with an offset in field magnitude, also seen in the field difference. In the high conductivity case (bottom row), we note a similar match between the analytic time decay and the hybrid east response; however, the clear exponential decay of the analytic response has an offset in magnitude, similar to the medium conductivity case. The radial and north components are close to 0 in all cases and match with theory. For observer #2, also located on the surface in the *xy* plane, but at 45° from the midnight meridian, we note that a different geometry appears within the field components. At this location, induced signals appear in both the east (green) and radial (blue) components. To first order, the hybrid response curves replicate the time decay of the analytic theory; how-

ever, we observe relatively large amplifications of the magnitude of the hybrid-modeled fields relative to the analytic theory. In particular, the magnitude of these excess amplifications can be more than a factor of 2 higher than the analytically calculated induced fields, especially in the high interior conductivity case.

The hybrid model time series can be used to determine the best-fit conductive radius and conductivity under the assumption that the hybrid fields are representative of only induced fields, essentially quantifying the error associated with using the vacuum approximation from Dyal and Parkin (1971). Color contours in Figure 3 show the root-mean-square error (RMSE) for a range of theoretical fits to the downstream hybrid magnetic fields as a function of the radius, R_1, and conductivity, σ_1, of the conducting body. The best-fit model in each combination of observer and conductivity is shown by the cyan circle, while the reference model is shown by the pink diamond (note that the reference radius is constant (1.6×10^6 m) for all cases). As seen in equations (1) –(4), the amplitude of the induced field depends only on the radius of the conductor, while the characteristic decay time is dependent on both the radius and conductivity of the interior. For observer #1 with $\sigma_1 = 10^{-4}$ S/m, the best-fit analytic model underpredicts the conducting radius due to the decreased amplitude of the hybrid model. The best-fit conductivity therefore must increase to compensate for the smaller core in order to match the correct decay time. For the other cases, the best-fit models overpredict the radius up to the maximum allowed value of 1,725 km. Given the overshoot of the magnetic field for these three cases as seen in the time series, the true minimum error fit most likely lies above 1,725 km. In turn, the best-fit conductivity is either below or near the expected value. In sum, the comparisons between the best-fit analytic models and the true expected values for the conducting radius and conductivity demonstrate that analysis of observed TDEM sounding without taking into account the presence of additional wake magnetic fields leads to errors in the retrievals of interior conductivity parameters.

5. Discussion and Conclusion

We have demonstrated the use of a time-dependent plasma hybrid model with variability in the upstream magnetic fields for the interpretation of the induced fields from a conducting lunar interior. The model results show some aspects that qualitatively agree with the "vacuum response" theory of Dyal and Parkin (1971), including an expansion of induced fields within the lunar wake region, confinement of induced fields on the upstream hemisphere of the Moon at or below the lunar crust, and approximately equal exponential decay periods of induced fields. In contrast, the model suggests that induced fields are typically enhanced in magnitude within the lunar wake over theoretical expectations. Physically, we interpret this as arising from two effects: (1) the presence of plasma-induced fields in the lunar wake that add constructively to the field strength and (2) the compression of induced fields into the lunar nightside that emerge from the lunar interior near the terminators by the solar wind ram pressure. Wake plasma fields are typically on the order of 20–30% of the ambient interplanetary magnetic field strength (e.g., Fatemi et al., 2013; Holmström & Fatemi, 2018; Zhang et al., 2014) although in extreme cases (i.e., high plasma β) can rise above 300–400% of the ambient field strength (Poppe et al., 2014). Compression of the induced fields near the lunar terminators by the solar wind ram pressure is also a significant cause of increased total fields observed in the hybrid model over the analytic solution. While not shown here, magnetic fields at the lunar surface continue to increase in magnitude over the analytic solution as the observer approaches the terminator, indicative of significant compression of induced fields by the solar wind. Finally, for locations on the lunar dayside, the solar wind ram pressure is sufficiently large to completely compress all induced fields below the surface such that no signature is observable. These findings confirm and extend previous, time-independent hybrid plasma simulations of the interaction between the solar wind and induced fields at the Moon (Fatemi et al., 2015).

Our results here also have broader implications for the study of geophysically induced EM fields within airless bodies across the solar system. In addition to the Moon, EM induction has been used as a tool at Mercury (Jia et al., 2015; Johnson et al., 2015) and the Galilean satellites (Kivelson et al., 2002; Lindkvist et al., 2015; Saur et al., 2014; Seufert et al., 2011; Zimmer et al., 2000) to study interior structure. These studies have generally demonstrated that inclusion of induced fields from the planetary interiors is critical in explaining in situ magnetic field measurements at these bodies (e.g., Khurana et al., 1998; Zimmer et al., 2000). For example, it has been shown that induced fields can influence the structure of the Alfvén wings and ionospheric currents at Europa (Neubauer, 1999; Schilling et al., 2007). While there are important differences between many of these objects and the case of the Moon in the solar wind, including the presence of internal fields (Mercury and Ganymede), significantly different upstream plasma and field conditions (Galilean satellites),

and the presence of conducting ionospheres and associated mass loading of the incident plasma (Galilean satellites), the model results shown here applied to the Moon further confirm that the inclusion of plasma interaction effects alongside inductive currents from a planetary interior yields results different than that from theory that assumes a vacuum response (e.g., Dyal & Parkin, 1971; Seufert et al., 2011).

Acknowledgments
H. F. H. gratefully acknowledges the NASA Earth and Space Science Fellowship Program, grant NNX14AP19H. A. R. P., S. F., and G. T. D. also acknowledge support from NASA's SSERVI Institute, grant NNX14AG16A, NASA's Solar System Workings program, grant 80NSSC17K0769, and NASA's Lunar Data Analysis Program, grant NNX16AN56G. The modeling results are publicly available at XXX (to be assigned after publication of paper).

References

Blank, J. L., & Sill, W. R. (1969). Response of the Moon to the time-varying interplanetary magnetic field. *Journal of Geophysical Research*, *74*(3), 736–743. https://doi.org/10.1029/JA074i003p00736

Canup, R. M., Visscher, C., Salmon, J., & Fegley, B. Jr. (2015). Lunar volatile depletion due to incomplete accretion within an impact-generated disk. *Nature Geoscience*, *8*, 918–921.

Ćuk, M., Hamilton, D. P., Lock, S. J., & Stewart, S. T. (2016). Tidal evolution of the Moon from a high-obliquity, high-angular-momentum Earth. *Nature*, *539*(7629), 402–406.

Dyal, P., & Parkin, C. W. (1971). Electrical conductivity and temperature of the lunar interior from magnetic transient-response measurements. *Journal of Geophysical Research*, *76*(25), 5947.

Dyal, P., Parkin, C. W., & Daily, W. D. (1974). Magnetism and the interior of the Moon. *Reviews of Geophysics and Space Physics*, *12*(4), 568–591.

Dyal, P., Parkin, C., & Daily, W. (1976). Structure of the lunar interior from magnetic field measurements. In *Lunar and Planetary Science Conference Proceedings*, pp. 3077–3095. Vol. 7.

Dyal, P., Parkin, C. W., & Daily, W. D. (1977). Global lunar crust: Electrical conductivity and thermoelectric origin of remanent magnetism. *Proceedings of the 8th Lunar Science Conference*, *8*, 767–783.

Fatemi, S., Fuqua, H. A., Poppe, A. R., Delory, G. T., Halekas, J. S., Farrell, W. M., & Holmström, M. (2015). On the confinement of lunar induced magnetic fields. *Geophysical Research Letters*, *42*, 6931–6938. https://doi.org/10.1002/2015GL065576

Fatemi, S., Holmström, M., Futaana, Y., Barabash, S., & Lue, C. (2013). The lunar wake current systems. *Geophysical Research Letters*, *40*, 17–21. https://doi.org/10.1029/2012GL054635

Fatemi, S., Poppe, A. R., Delory, G. T., & Farrell, W. M. (2017). AMITIS: A 3D GPU-based hybrid-PIC Model for space and plasma physics. *Journal of Physics: Conference Series*, *837*, 012017.

Grimm, R. E. (2013). Geophysical constraints on the lunar Procellarum KREEP Terrane. *Journal of Geophysical Research: Planets*, *118*, 768–778. https://doi.org/10.1029/2012JE004114

Grimm, R. E., & Delory, G. T. (2012). Next-generation electromagnetic sounding of the Moon. *Advances in Space Research*, *50*(12), 1687–1701.

Halekas, J. S., Saito, Y., Delory, G. T., & Farrell, W. M. (2011). New views of the lunar plasma environment. *Planetary and Space Science*, *59*, 1681–1694.

Holmström, M., & Fatemi, S. (2018). *Current systems of inert moons*. (Chap. 29, pp. 497–512). Washington, DC: American Geophysical Union (AGU). https://doi.org/10.1002/9781119324522.ch29

Holmström, M., Fatemi, S., Futaana, Y., & Nilsson, H. (2012). The interaction between the Moon and the solar wind. *Earth Planets Space*, *64*, 237–245.

Hood, L., Herbert, F., & Sonett, C. (1982). The deep lunar electrical conductivity profile: Structural and thermal inferences. *Journal of Geophysical Research*, *87*(B7), 5311–5326.

Hood, L. L., Mitchell, D. L., Lin, R. P., Acuña, M. H., & Binder, A. B. (1999). Initial measurements of the lunar induced magnetic dipole moment using Lunar Prospector Magnetometer data. *Geophysical Research Letters*, *26*(15), 2327–2330.

Jaumann, R., Hiesinger, H., Anand, M., Crawford, I., Wagner, R., Sohl, F., et al. (2012). Geology, geochemistry, and geophysics of the Moon: Status of current understanding. *Planetary and Space Science*, *74*(1), 15–41.

Jia, X., Slavin, J. A., Gombosi, T. I., Daldorff, L. K. S., Toth, G., & van der Holst, B. (2015). Global MHD simulations of Mercury's magnetosphere with coupled planetary interior: Induction effect of the planetary conducting core on the global interactions. *Journal of Geophysical Research: Space Physics*, *120*, 4763–4775. https://doi.org/10.1002/2015JA021143

Johnson, C. L., Philpott, L. C., Anderson, B. J., Korth, H., Hauck, S. A. II, Heyner, D., et al. (2015). MESSENGER observations of induced magnetic fields in Mercury's core. *Geophysical Research Letters*, *43*, 2436–2444. https://doi.org/10.1002/2015GL067370

Jolliff, B. L., Gillis, J. J., Haskin, L. A., Korotev, R. L., & Wieczorek, M. A. (2000). Major lunar crustal terranes: Surface expressions and crust-mantle origins. *Journal of Geophysical Research*, *105*(E2), 4197–4216.

Kallio, E. (2005). Formation of the lunar wake in quasi-neutral hybrid model. *Geophysical Research Letters*, *32*, L06107. https://doi.org/10.1029/2004GL021989

Khan, A., Connolly, J., Olsen, N., & Mosegaard, K. (2006). Constraining the composition and thermal state of the Moon from an inversion of electromagnetic lunar day-side transfer functions. *Earth and Planetary Science Letters*, *248*(3-4), 579–598.

Khurana, K. K., Jia, X., Kivelson, M. G., Nimmo, F., Schubert, G., & Russell, C. T. (2011). Evidence of a global magma ocean in Io's interior. *Science*, *332*(6034), 1186–1189. https://doi.org/10.1126/science.1201425

Khurana, K. K., Kivelson, M. G., Hand, K. P., & Russell, C. T. (2009). *Electromagnetic induction from Europa's ocean and the deep interior*. (pp. 572–586). Tuscon: University of Arizona Press.

Khurana, K., Kivelson, M., Stevenson, D., Schubert, G., Russell, C., Walker, R., & Polanskey, C. (1998). Induced magnetic fields as evidence for subsurface oceans in Europa and Callisto. *Nature*, *395*(6704), 777–780.

Kirkici, H., Rose, M. F., & Chaloupka, T. (1996). Experimental study on simulated lunar soil: High voltage breakdown and electrical insulation characteristics. *IEEE Transactions on Dielectrics and Electrical Insulation*, *3*(1), 119–125.

Kivelson, M. G., Khurana, K. K., & Volwerk, M. (2002). The permanent and inductive magnetic moments of Ganymede. *Icarus*, *157*, 507–522.

Lindkvist, J., Holmström, M., Khurana, K. K., Fatemi, S., & Barabash, S. (2015). Callisto plasma interactions: Hybrid modeling including induction by a subsurface ocean. *Journal of Geophysical Research: Space Physics*, *120*, 4877–4889. https://doi.org/10.1002/2015JA021212

Lipatov, A., Cooper, J., Paterson, W., Sittler, E. Jr., Hartle, R., & Simpson, D. G. (2013). Jovian plasma torus interaction with Europa. Plasma wake structure and effect of inductive magnetic field: 3D hybrid kinetic simulation. *Planetary and Space Science*, *77*, 12–24.

Lock, S. J., & Stewart, S. T. (2017). The structure of terrestrial bodies: Impact heating, corotation limits, and synestias. *Journal of Geophysical Research: Planets*, *122*, 950–982. https://doi.org/10.1002/2016JE005239

Lock, S. J., Stewart, S. T., Petaev, M. I., Leinhardt, Z., Mace, M. T., Jacobsen, S. B., & Cuk, M. (2018). The origin of the Moon within a terrestrial synestia. *Journal of Geophysical Research: Planets*, *123*, 910–951. https://doi.org/10.1002/2017JE005333

Neubauer, F. M. (1999). Alfvén wings and electromagnetic induction in the interiors: Europa and Callisto. *Journal of Geophysical Research*, *104*(A12), 28,671–28,684.

Oran, R., Weiss, B. P., & Cohen, O. (2018). Were chondrites magnetized by the early solar wind? *Earth and Planetary Science Letters*, *492*, 222–231.

Poppe, A. R., Fatemi, S., Halekas, J. S., Holmström, M., & Delory, G. T. (2014). ARTEMIS observations of extreme diamagnetic fields in the lunar wake. *Geophysical Research Letters*, *41*, 3766–3773. https://doi.org/10.1002/2014GL060280

Russell, C. T., Coleman, P. J. Jr., & Goldstein, B. E. (1981). Measurements of the lunar induced magnetic moment in the geomagnetic tail: Evidence for a lunar core? *Proceedings of the Lunar and Planetary Science*, *12B*, 831–836.

Saur, J., Duling, S., Roth, L., Jia, X., Strobel, D. F., Feldman, P. D., et al. (2014). The search for a subsurface ocean in Ganymede with Hubble Space Telescope observations of its auroral ovals. *Journal of Geophysical Research: Space Physics*, *120*, 1715–1737. https://doi.org/10.1002/2014JA020778

Saur, J., Neubauer, F. M., & Glassmeier, K.-H. (2010). Induced magnetic fields in solar system bodies. *Space Science Reviews*, *152*(1), 391–421.

Schilling, N., Neubauer, F. M., & Saur, J. (2007). Time-varying interaction of Europa with the Jovian magnetosphere: Constraints on the conductivity of Europa's subsurface ocean. *Icarus*, *192*(1), 41–55.

Schubert, G., & Schwartz, K. (1969). A theory for the interpretation of lunar surface magnetometer data. *The Moon*, *1*(1), 106–117.

Schubert, G., Smith, B. F., Sonett, C. P., Colburn, D. S., & Schwartz, K. (1973). Night side electromagnetic response of the Moon. *Journal of Geophysical Research*, *78*(19), 3688–3696.

Schwartz, K., & Schubert, G. (1973). Lunar electromagnetic scattering I. Propagation parallel to the diamagnetic cavity axis. *Journal of Geophysical Research*, *78*(28), 6496–6506.

Seufert, M., Saur, J., & Neubauer, F. M. (2011). Multi-frequency electromagnetic sounding of the Galilean moons. *Icarus*, *214*(2), 477–494. https://doi.org/10.1016/j.icarus.2011.03.017

Shimizu, H., Matsushima, M., Takahashi, F., Shibuya, H., & Tsunakawa, H. (2013). Constraint on the lunar core size from electromagnetic sounding based on magnetic field observations by an orbiting satellite. *Icarus*, *222*(1), 32–43.

Sonett, C. P. (1982). Electromagnetic induction in the Moon. *Reviews of Geophysics and Space Physics*, *20*(3), 411–455.

Sonett, C. P., & Colburn, D. S. (1967). Establishment of a lunar unipolar generator and associated shock and wake by the solar wind. *Nature*, *216*, 340–343.

Sonett, C. P., & Colburn, D. S. (1968). The principle of solar wind induced planetary dynamos. *Physics of the Earth and Planetary Interiors*, *1*, 326–346.

Strangway, D. W., Chapman, W. B., Olhoeft, G. R., & Carnes, J. (1972). Electrical properties of lunar soil dependence on frequency, temperature and moisture. *Earth and Planetary Science Letters*, *16*, 275–281.

Vernisse, Y., Kriegel, H., Wiehle, S., Motschmann, U., & Glassmeier, K.-H. (2013). Stellar winds and planetary bodies simulations: Lunar type interaction in super-Alfvénic and sub-Alfvénic flows. *Planetary and Space Science*, *84*, 37–47.

Wang, Y.-C., Müller, J., Ip, W.-H., & Motschmann, U. (2011). A 3D hybrid simulation study of the electromagnetic field distributions in the lunar wake. *Icarus*, *216*(2), 415–425. https://doi.org/10.1016/j.icarus.2011.09.021

Weber, R. C., Lin, P.-Y., Garnero, E. J., Williams, Q., & Lognonne, P. (2011). Seismic detection of the lunar core. *Science*, *331*(6015), 309–312.

Wieczorek, M. A., Jolliff, B. L., Khan, A., Pritchard, M. E., Weiss, B. P., Williams, J. G., et al. (2006). The constitution and structure of the lunar interior. *Reviews in Mineralogy and Geochemistry*, *60*(1), 221–364.

Wieczorek, M. A., Neumann, G. A., Nimmo, F., Kiefer, W. S., Taylor, G. J., Melosh, H. J., et al. (2013). The crust of the Moon as seen by GRAIL. *Science*, *339*(6120), 671–675. https://doi.org/10.1126/science.1231530

Zhang, H., Khurana, K. K., Kivelson, M. G., Angelopoulos, V., Wan, W. X., Liu, L. B., et al. (2014). Three-dimensional lunar wake reconstructed from ARTEMIS data. *Journal of Geophysical Research: Space Physics*, *119*, 5220–5243. https://doi.org/10.1002/2014JA020111

Zhang, H., Khurana, K. K., Zong, Q.-G., Kivelson, M. G., Hsu, T.-S., Wan, W. X., et al. (2012). Outward expansion of the lunar wake: ARTEMIS observations. *Geophysical Research Letters*, *39*, L18104. https://doi.org/10.1029/2012GL052839

Zimmer, C., Khurana, K. K., & Kivelson, M. G. (2000). Subsurface oceans on Europa and Callisto: Constraints from Galileo Magnetometer Observations. *Icarus*, *147*, 329–347.